# Numerical Simulation of the Poiseuille-Rayleigh-Bénard Instability for a Supercritical Fluid in a Mini-channel

Djilali Ameur, Isabelle Raspo

# NUMERICAL SIMULATION OF THE POISEUILLE-RAYLEIGH-BÉNARD

# INSTABILITY FOR A SUPERCRITICAL FLUID IN A MINI-CHANNEL

D. Ameur [1] and I. Raspo[2]

M2P2, U.M.R. 7340 C.N.R.S.,

Aix-Marseille University,

Technopôle de Château-Gombert,

38 rue F. Joliot Curie, 13451 Marseille Cedex 20, France

[1]e-mail address: ameur@L3m.univ-mrs.fr

[2]e-mail address: isabel@l3m.univ-mrs.fr

Corresponding author: D. Ameur

**ABSTRACT**

The Poiseuille-Rayleigh-Bénard problem, involving the onset of thermoconvective structures in channels heated from below, was the subject of many theoretical, numerical and experimental studies for incompressible flows or perfect gas. However, to the authors' knowledge, this problem was never studied for supercritical fluids. The objective of this paper is to study the influence of the specific properties of such fluids on thermoconvective instability phenomena compared with those observed in the perfect gas case. The effect of the distance to the critical point is also investigated. The numerical approach used is based on the Navier-Stokes equations in the framework of the low Mach number approximation.

**KEY WORDS:** thermoconvective instability, convective instability, absolute instability, mixed convection flows, spectral method, low Mach number approximation

## NOMENCLATURE

| | | |
|---|---|---|
| $a$ | [-] | Energy parameter in the equation of state |
| $b$ | [-] | Covolume in the equation of state |
| $C_P{'}$ | [J/(kg.K)] | Isobaric specific heat |
| $C_V{'}$ | [J/(kg.K)] | Isochoric specific heat |
| $g'$ | [m/s$^2$] | Gravity constant |
| $H'$ | [m] | Channel height |
| $L'$ | [m] | Channel length |
| $P'$ | [Pa] | pressure |
| $R'$ | [J/(kg.K)] | Perfect gas constant |
| $t'$ | [s] | Time |
| $T'$ | [K] | Temperature |
| $u'$ | [m/s] | Velocity component in the x-direction |
| $v'$ | [m/s] | Velocity component in the y-direction |
| $x'$ | [m] | Cartesian axis direction |
| $y'$ | [m] | Cartesian axis direction |

**Special characters**

| | | |
|---|---|---|
| $\alpha$ | [-] | Soave function in the equation of state |
| $\beta'$ | [K$^{-1}$] | Thermal expansion coefficient |

| $\delta t$ | [-] | Dimensionless time step |
|---|---|---|
| $\delta T'$ | [K] | Temperature increase |
| $\varepsilon$ | [-] | Dimensionless proximity to the critical point, $\varepsilon = \left(T_i' - T_c'\right)/T_c'$ |
| $\lambda'$ | [W/(m.K)] | Thermal conductivity |
| $\mu'$ | [Pa.s] | Dynamic viscosity |
| $\rho'$ | [kg/m³] | Density |
| $\chi'$ | [Pa$^{-1}$] | Isothermal compressibility |
| $\omega$ | [-] | Acentric factor |
| $\Omega$ | [-] | Computational domain |
| $\partial\Omega$ | [-] | Boundary of the computational domain |
| $\gamma$ | [-] | Specific heats ratio |

**Subscripts**

| | |
|---|---|
| *b* | Background property |
| *c* | Critical property |
| *dyn* | Dynamic part |
| *hyd* | Hydrostatic part |
| *i* | Initial value |
| *mean* | Mean value |
| *ref* | Reference value |
| *th* | Thermodynamic part |
| 0 | Value for the perfect gas |

## 1. INTRODUCTION

Poiseuille-Rayleigh-Bénard (PRB) flows are mixed convection flows in horizontal channels heated from below. When the Rayleigh number exceeds a critical value, thermoconvective structures develop in the channel. This paper focuses on these thermal instabilities in the case of fluids near their gas-liquid critical point. More precisely, a supercritical fluid (SCF) is a fluid for which temperature and pressure are larger than those of the critical point. In this zone of the phase diagram, the physical properties of the fluid (density, viscosity, diffusivity) are intermediate between those of liquids and gases. Moreover, they are very sensitive to temperature and pressure variations. These tunable properties motivated the use of SCF in many industrial applications, such as supercritical fluid extraction (Reverchon and De Marco, 2006), particle generation (Cocero et al., 2009), in particular in pharmaceutical industry, and preparation of metallic films using supercritical fluid deposition (Erkey, 2009).

The instability onset and the development of the associated patterns in PRB flows were extensively studied for incompressible fluids and perfect gas from many years because the PRB configuration is relevant for several technological processes such as the cooling of microelectronic equipments (Incropera, 1988) or the growth of thin crystal films from chemical vapor deposition (CVD) (Evans and Greif, 1989; Evans and Greif, 1991; Evans and Greif, 1993; Spall, 1996). A detailed review of various studies reported in literature was performed by Nicolas (2002). These studies showed that when the base flow becomes unstable, two kinds of thermoconvective structures may appear: transversal rolls at low Reynolds number (about *Re*<10) and longitudinal rolls at higher Reynolds number. The transversal rolls axes are perpendicular to the mean flow direction and these patterns can be considered as a quasi two-dimensional structure, whereas the longitudinal rolls axes are parallel to the mean flow and the three velocity components are excited. Results of linear

stability analysis for incompressible flows showed that the transversal rolls are due to a convective or an absolute instability depending on the value of the Rayleigh number (Müller et al., 1992; Carrière and Monkewitz, 1999). When the flow is convectively unstable, the initial perturbation locally grows, it moves downstream and it finally leaves the system. Hence, the rolls cross the channel during time and the flow becomes stable again once they moved away. On the other hand, in the case of absolute instability, the initial perturbation locally grows but it also expands in the whole system so that the rolls appear throughout the channel all the time although they move downstream: when a roll moves away, another one is locally generated in its place by the perturbation. The convective or absolute nature of the instability depends on the value of the Rayleigh number $Ra$, as is shown by the stability diagram in the plane $Ra$-$Re$ (Fig. 1). The critical Rayleigh numbers for the onset of convective instability, $Ra_{c1}$, and for the onset of absolute instability, $Ra_{c2}$, are computed from the formulae of Müller et al. (1992) for a Prandtl number $Pr$=0.6567 (corresponding to the value for $CO_2$ as a perfect gas). It can be seen that they both increase with the Reynolds number. On the other hand, Carrière and Monkewitz (1999) showed that the longitudinal rolls can only be convectively unstable and that the critical Rayleigh number is independent of $Re$ and $Ra$. These theoretical predictions were confirmed by experiments.

To the authors' knowledge, the PRB problem was never studied for fluids near their liquid-gas critical point while it is relevant for supercritical fluid deposition processes and it can be expected that the fluid response to the bottom boundary heating may be quite different in this special zone of the phase diagram. Indeed, as was already said, near the critical point, thermodynamic properties, such as density, and transport coefficients exhibit large variations with temperature and pressure. More precisely, on the critical isochore, several properties, such as isothermal compressibility, thermal expansion coefficient, specific heats or thermal conductivity, diverge as the critical temperature is approached, while other properties, such as

thermal diffusivity, tend to zero. These critical behaviors cause some peculiar phenomena in supercritical fluids, such as a fast heat transport by thermoacoustic effects (also called Piston effect) (Onuki et al., 1990; Boukari, 1990; Zappoli et al., 1990). Natural convection in SCF was extensively studied in the past decade (Zappoli et al., 1996; Chiwata and Onuki, 2001; Amiroudine et al., 2001; Furukawa and Onuki, 2002; Furukawa et al., 2003; Amiroudine and Zappoli, 2003; Raspo et al., 2004; Accary et al., 2004; Accary et al., 2005a; Accary et al., 2005b; Gorbunov et al., 2007), especially in the Rayleigh-Bénard configuration (Amiroudine et al., 2001; Furukawa and Onuki, 2002; Furukawa et al., 2003; Amiroudine and Zappoli, 2003; Raspo et al., 2004; Accary et al., 2004; Accary et al., 2005a; Accary et al., 2005b; Gorbunov et al., 2007). These works showed, in particular, that the adiabatic temperature gradient, which is generally relevant only at large length scale, like for the study of atmospheric flows, must be taken into account for the convection onset in supercritical fluids in cavities of a few millimeters in height. We can therefore suppose that the specific properties of SCF may also modify the instability onset in the PRB configuration.

In the present paper, the stability of a supercritical fluid, modeled by the Peng-Robinson equation of state, in the PRB configuration is investigated using 2D direct numerical simulations. The first section is devoted to the mathematical formulation of the treated problem, namely the Navier-Stokes equations in the framework of the low Mach number approximation and the boundary conditions. Then, the numerical method, based on a Chebyshev collocation approximation, is described in details. Results obtained for a Reynolds number equal to 50.57 in a channel of height $H'$=1mm are presented in the third section. First, we studied the influence of the temperature increase on the onset and the development of convection for a fluid set at 1K above its critical temperature. The relation between the Rayleigh number and the instability characteristics is thus investigated. In a

second part, we are focusing on the influence of the proximity to the critical point on the instability onset.

## 2. PHYSICAL PROBLEM AND MODELLING

The physical model consists of a 2D channel of height $H'$=1mm, with an aspect ratio $L'/H'$=10 or 15. The carried fluid is supercritical $CO_2$ subject to gravity. Initially, the fluid is at a uniform temperature slightly above the critical temperature, $T_i'=(1+\varepsilon)T_c'$ (with $\varepsilon \ll 1$), and at a mean density equal to the critical density $\rho_c'$, and it flows through the channel according to a Poiseuille profile. Then, the temperature of the bottom wall is gradually increased up to $T_{ch}'=T_i'+\delta T'$ (with $\delta T'$ ranging from about ten to some hundreds milliKelvin) from a distance $H'$ from inlet (see Fig. 2).

The supercritical fluid is modeled by the Peng-Robinson equation of state. This equation implicitly accounts for the divergence of the thermal expansion coefficient $\beta'$, of the isothermal compressibility $\chi'$ and of the specific heat at constant pressure $C_P'$ near the liquid-gas critical point. The divergence of the thermal conductivity $\lambda'$ is modelled by the formula $\lambda' = \lambda_b'[1+\Lambda(T'/T_c'-1)^{-0.5}]$. The physical parameters of $CO_2$ were used: $T_c'$=304.13K, $\rho_c'$=467.8kg.m$^{-3}$, $\lambda_b'$=0.04412W.m$^{-1}$.K$^{-1}$, $\Lambda$=0.75.

The evolution of the flow is governed by the time-dependent 2D Navier-Stokes equations coupled with the energy and the Peng-Robinson equations. These equations are solved in the framework of the low Mach number approximation (Paolucci, 1982): the pressure $P'$ is thus split into a thermodynamic part, $P_{th}'$, which is constant in space and appears in the energy equation and in the equation of state, and a dynamic part, $P_{dyn}'$, involved in the momentum equation. However, the basic approximation of Paolucci (1982) is modified as proposed in Accary et al. (2005c) to account for the stratification of the fluid near the critical point since

$Ma^2/Fr$ (where *Ma* and *Fr* are respectively the Mach and the Froud numbers) is not in

$O(Ma^2)$. We chose as characteristic variables $T_c'$ for temperature, $\rho_c'$ for density, $\rho_c'R'T_c'$ for

pressure (with $R'=188.92\text{J.kg}^{-1}.\text{K}^{-1}$ the perfect gas constant), $H'$ for length, $U'_{ref} = \sqrt{\beta'g'\delta T'H'}$

for velocity (with *g'* the Earth gravity), $H'/U'_{ref}$ for time and $\lambda_b'$ for thermal conductivity.

The specific heat at constant volume $C_V'$ and the dynamic viscosity $\mu'$ were fixed to their

background values, $C_{Vb}'=472.313\text{J.kg}^{-1}.\text{K}^{-1}$ and $\mu_b'=3.2702\times10^{-5}\text{Pa.s}$. The dimensionless

governing equations are therefore:

$$\frac{\partial \rho}{\partial t} + \nabla.(\rho\mathbf{V}) = 0 \tag{1}$$

$$\rho\frac{\partial \mathbf{V}}{\partial t} + \rho\mathbf{V}.\nabla\mathbf{V} = -\nabla P_{dyn} + \sqrt{\frac{Pr}{Ra}}\left[\Delta\mathbf{V} + \frac{1}{3}\nabla(\nabla.\mathbf{V})\right] - \frac{1}{Fr}(\rho-\rho_i)\mathbf{e}_y \tag{2}$$

$$\rho\frac{\partial T}{\partial t} + \rho\mathbf{V}.\nabla T = -(\gamma_0-1)T\left(\frac{\partial P}{\partial T}\right)_\rho (\nabla.\mathbf{V}) + \frac{\gamma_0}{Pr_0}\sqrt{\frac{Pr}{Ra}}\nabla.(\lambda\nabla T) \tag{3}$$

$$P_{th} + P_{hyd} = \frac{\rho T}{1-b\rho} - \frac{a\,\alpha(T)\rho^2}{1+2b\rho-b^2\rho^2} \tag{4}$$

with *a* and *b* the dimensionless energy parameter and covolume respectively and $\alpha$ the Soave

function defined by:

$$a = 1.487422 \;, b = 0.253076 \;, \alpha(T) = \left[1+m\left(1-\sqrt{T}\right)\right]^2$$

where *m* is computed from the acentric factor $\omega$ ($\omega$=0.225 for $CO_2$) by the formula

$$m = 0.37464 + 1.54226\omega - 0.26992\omega^2 \,.$$

In Eqs. (1)-(4), $P_{hyd}$ is the hydrostatic pressure introduced by the modification of the Low Mach number approximation (Accary et al., 2005c), $\mathbf{e}_y$ is the unit vector in the $y$-direction and $\gamma_0$ and $Pr_0$ are respectively the specific heats ratio and the Prandtl number for the perfect gas ($\gamma_0=1.4$, $Pr_0=0.6567$). The other dimensionless numbers introduced are the Prandtl number $Pr$, the Rayleigh number $Ra$, the Mach number $Ma$ and the Froud number $Fr$ which are defined by:

$$Pr = \frac{C_P' \mu_b'}{\lambda_b'} \;,\; Ra = \frac{\beta' g' \rho_c'^2 C_P' \delta T' H'^3}{\mu_b' \lambda_b'} \;,\; Ma = \frac{U_{ref}'}{\sqrt{\gamma_0 R' T_c'}} \;,\; Fr = \frac{U_{ref}'^2}{g' H'} \,.$$

In the above formula, the physical parameters $\beta'$ and $C_P'$ are calculated for the initial state ($T_i'$, $\rho_i'$) from the equation of state. The initial condition for the dimensionless variables in $\Omega = [0, L'/H'] \times [0,1]$ is:

$$u_i(x,y) = 1.5 Re \sqrt{\frac{Pr}{Ra}} \left[ 1 - (2y-1)^2 \right] \;,\; v_i(x,y) = 0 \tag{5}$$

where $Re$ is the Reynolds number defined by $Re = \rho_c' U_{mean}' H' / \mu_b'$, with $U'_{mean}$ the mean velocity at inlet,

$$T_i(x,y) = 1 + \varepsilon \tag{6}$$

and, as it was proposed in Accary et al. (2005c), the stratification of the fluid is taken into account leading to the initial condition for density and pressure:

$$\rho_i(x,y) = K_2 \frac{e^{-K_2 y}}{1 - e^{-K_2}} \tag{7}$$

$$P_i(x,y) = P_{thi} + P_{hyd}(y) \tag{8}$$

with $K_2 = \gamma_0 \dfrac{Ma^2}{K_1 Fr}$, $K_1 = \dfrac{1+\varepsilon}{(1-b)^2} - \dfrac{2a(1+b)\alpha(T_i)}{\left(1+2b-b^2\right)^2}$

and:

$$P_{thi} = \frac{1+\varepsilon}{1-b} - \frac{a\,\alpha(T_i)}{1+2b-b^2} \quad , \quad P_{hyd}(y) = K_1\left[K_2\frac{e^{-K_2 y}}{1-e^{-K_2}} - 1\right]$$

Equations (1)-(4) are solved with the following boundary conditions:

- On the channel walls, the no-slip condition is prescribed for the velocity. The top wall ($y=1$) is kept at the initial temperature $T_i$. On the bottom heated wall ($y=0$), in order to avoid a discontinuity of the temperature profile, the following boundary condition is imposed for $0 \leq x \leq L'/H'$:

$$T(x,0,t) = T_i + \delta T\left[th(2x-2) - th(-2)\right]/\left[th(18) - th(-2)\right] \tag{9}$$

This boundary condition allows a continuous transition between the cold entry zone for $0 \leq x \leq 1$ and the hot zone for $1 \leq x \leq L'/H'$.

- At the channel inlet ($x=0$), temperature is kept at its initial value $T_i$ and a parabolic profile is imposed for velocity:

$$
\begin{aligned}
T(0,y,t) &= T_i = 1+\varepsilon \\
u(0,y,t) &= 1.5Re\sqrt{\frac{Pr}{Ra}}\left[1-(2y-1)^2\right] \quad , \quad v(0,y,t) = 0
\end{aligned}
\tag{10}
$$

- At the channel outlet ($x=L'/H'$), an Orlanski type boundary condition is prescribed for all the variables:

$$\frac{\partial \phi}{\partial t} + Re\sqrt{\frac{Pr}{Ra}}\frac{\partial \phi}{\partial x} = 0 \quad \text{for} \quad \phi = T, u, v. \tag{11}$$

### 3. NUMERICAL METHOD

### 3.1. Time scheme and space approximation

Equations (1)-(4) are discretized in time with a second order semi-implicit scheme: the convective terms are evaluated by an Adams-Bashforth scheme, a second order backward Euler scheme is used for the discretization of time derivatives and the diffusive terms as the energy source term $-T\left(\partial P/\partial T\right)_{\rho}\left(\nabla.\mathbf{V}\right)$ are implicitly treated. The outlet boundary condition (11) is also discretized using the same second order scheme, leading to a Dirichlet boundary condition for the variables at the current time step *n+1*.

The space approximation is performed using a Chebyshev-collocation method with Gauss-Lobatto points. For the computation of the convective terms, the derivatives are calculated in the spectral space and the products are performed in the physical one; the connection between the spectral and the physical spaces is realized through a FFT algorithm. On the other hand, the spectral differentiation matrices are used for the derivatives in the diffusive terms.

### 3.2. Numerical algorithm

At a given time step, the discretized equations are coupled because of the implicit treatment of the energy source term involving $\nabla.\mathbf{V}$. This term must be implicitly evaluated for supercritical fluids. However, it is possible to completely uncouple the solution of the energy equation and the computation of the dynamic field by calculating the velocity divergence from the sole knowledge of the thermodynamic variables (Ouazzani and Garrabos, 2007; Raspo and Ouazzani, 2009). The procedure consists in taking the total derivative of the equation of state (4) written in the form $F(P_{th}, T, \rho)=0$. Then, using the energy equation (3) and the continuity equation (1), the following formula is obtained for the velocity divergence:

$$\nabla . \mathbf{V} = \frac{\dfrac{dP_{th}}{dt} + \dfrac{\gamma_0}{Pr_0}\sqrt{\dfrac{Pr}{Ra}}\,\dfrac{1}{\rho}\left(\dfrac{\partial F}{\partial T}\right)_{\rho,P_{th}} \nabla.(\lambda \nabla T)}{\rho\left(\dfrac{\partial F}{\partial \rho}\right)_{T,P_{th}} + (\gamma_0 - 1)\dfrac{T}{\rho}\left(\dfrac{\partial P_{th}}{\partial T}\right)_{\rho}\left(\dfrac{\partial F}{\partial T}\right)_{\rho,P_{th}}} \tag{12}$$

with:

$$\frac{1}{\rho}\left(\frac{\partial F}{\partial T}\right)_{\rho,P_{th}} = -\frac{1}{1-b\rho} + \frac{a\rho}{1+2b\rho - b^2\rho^2}\frac{d\alpha}{dT} \; ,$$

$$\left(\frac{\partial F}{\partial \rho}\right)_{T,P_{th}} = -\frac{T}{(1-b\rho)^2} + \frac{2a\,\alpha(T)(1+b\rho)\rho^2}{\left(1+2b\rho - b^2\rho^2\right)^2} \; ,$$

$$T\left(\frac{\partial P_{th}}{\partial T}\right)_{\rho} = P_{th} + P_{hyd} - a\left(T\frac{d\alpha}{dT} - \alpha\right)\frac{\rho^2}{1+2b\rho - b^2\rho^2} \; .$$

In the case of an open system, as the one considered here, the thermodynamic pressure $P_{th}$ is also constant in time. Therefore, the time derivative $dP_{th}/dt$ disappears in Eq. (12). Otherwise, this derivative can be evaluated using a second order backward Euler scheme as in Raspo and Ouazzani (2009).

Thanks to Eq. (12), the discretized equations are solved in two successive steps: first, the thermodynamic variables are computed through an iterative algorithm (Ouazzani and Garrabos, 2007; Raspo and Ouazzani, 2009) and then the Navier-Stokes equations are solved using the modified projection method developed in Hugues and Randriamampianina (1998) and extended to variable density flows. The two steps are described in detail below.

- 1st step: Computation of ($T, \rho, \nabla.\mathbf{V}$)

At time step $n+1$, the discretized energy equation can be written as a Helmholtz equation with coefficients involving $\lambda^{n+1}$ and $\rho^{n+1}$. In order to take advantage of the efficiency of the full diagonalization technique developed for the solution of Helmholtz problems with time-

independent coefficients (Haldenwang et al., 1984), the density and the thermal conductivity are split into a constant part, namely their value at $t=0$, and a time-dependent part. So, the terms involving the time-dependent parts are treated as source terms and the discretized energy equation can be written as a Helmholtz equation with constant coefficients. The complete diagonalization of the Helmholtz operator with constant coefficients is performed once for all in a preprocessing stage. Then, at each time step, the solution of the Helmholtz problem is reduced to matrix products, leading to a very efficient solution technique on supercomputers.

More precisely, the computation of $T$, $\rho$ and $\nabla.\mathbf{V}$ is performed through the following iterative algorithm:

1. The variables $T^{k-1}$, $\rho^{k-1}$ and $(\nabla.\mathbf{V})^{k-1}$ are initialized at their values at the previous time step $n$;

2. The temperature $T^k$ is obtained by the solution of the Helmholtz equation:

$$\frac{\gamma_0}{Pr_0}\sqrt{\frac{Pr}{Ra}}\lambda_i \Delta T^k - \frac{3}{2\delta t}\rho_i T^k = \left(\rho^{k-1}-\rho_i\right)\frac{3\,T^{k-1}}{2\delta t} - \frac{\gamma_0}{Pr_0}\sqrt{\frac{Pr}{Ra}}\nabla.\left(\left(\lambda^{k-1}-\lambda_i\right)\nabla T^{k-1}\right)$$

$$+\left(\gamma_0-1\right)T^{k-1}\left(\frac{\partial P_{th}}{\partial T}\right)_\rho^{k-1}\left(\nabla.V\right)^{k-1} - \rho^{k-1}\left(\frac{4T^n-T^{n-1}}{2\delta t}\right)$$

$$+AB\left(\rho\mathbf{V}.\nabla T\right)^{n,n-1}$$

with the boundary conditions of the problem. In the above equation, $\delta t$ is the time-step and the notation $AB(.)$ means an Adams-Bashforth evaluation of the quantity:

$$AB\left(\phi\right)^{n,n-1} = 2\phi^n - \phi^{n-1}$$

3. The thermal conductivity $\lambda^k$ is updated;

4. The density $\rho^k$ is computed from the equation of state (4);

5. The velocity divergence $(\nabla.\mathbf{V})^k$ is computed by Eq. (12).

13

The steps 2 to 5 are repeated until convergence is achieved on temperature and density. The convergence criterion used is Max*(ResT,Resρ)*<10⁻¹¹, with *Resφ*=Max*((φ^k-φ^{k-1})/φ^{k-1})* for $\phi=T,\rho$ and the maximum number of iterations is fixed to 150.

- 2$^{nd}$ step: Computation of (**V**, $P_{dyn}$)

When starting the solution of the Navier-Stokes equations, temperature, density and velocity divergence at the current time step *n+1* are known. It is therefore possible to use a projection-type algorithm such as those developed for the solution of incompressible Navier-Stokes equations, with some modifications. In this work, we have used the modified projection method proposed by Hugues and Randriamampianina (1998) and analysed in details in Raspo et al. (2002). It was shown in particular that the modification introduced by Hugues and Randriamampianina, namely the computation of a preliminary pressure, improves the accuracy on pressure and allows to reduce the slip velocity compared to other projection methods (Raspo et al., 2002). The modified projection method consists in solving the Navier-Stokes equations by three successive steps as follows:

- *Computation of a preliminary pressure*

First, a preliminary pressure $\bar{P}_{dyn}^{n+1}$ is computed from a Poisson equation derived from the discretized momentum equation (2):

$$\Delta\bar{P}_{dyn}^{n+1} = \nabla.\left[ -AB\left(\rho\mathbf{V}.\nabla\mathbf{V}\right)^{n,n-1} + \rho^{n+1}\left(\frac{4\mathbf{V}^n - \mathbf{V}^{n-1}}{2\delta t}\right) + \frac{1}{3}\sqrt{\frac{Pr}{Ra}}\nabla\left(\nabla.\mathbf{V}\right)^{n+1} - \frac{1}{Fr}\left(\rho^{n+1}-\rho_i\right)\mathbf{e}_y \right]$$
$$+ \sqrt{\frac{Pr}{Ra}}\Delta\left(\nabla.\mathbf{V}\right)^{n+1} + \frac{3}{2\delta t}\left(\frac{3\rho^{n+1} - 4\rho^n + \rho^{n-1}}{2\delta t}\right)$$

Neumann boundary conditions are obtained by the normal projection of the momentum equation (2) on the boundary:

$$\frac{\partial \overline{P}_{dyn}^{n+1}}{\partial n} = \mathrm{n.} \left[ -AB\left(\rho \mathbf{V}.\nabla \mathbf{V}\right)^{n,n-1} + \rho^{n+1} \left( \frac{-3\mathbf{W}^{n+1} + 4\mathbf{V}^n - \mathbf{V}^{n-1}}{2\delta t} \right) + \frac{4}{3}\sqrt{\frac{Pr}{Ra}} \nabla\left(\nabla.\mathbf{V}\right)^{n+1} \right.$$

$$\left. -\frac{1}{Fr}\left(\rho^{n+1} - \rho_i\right)\mathbf{e}_y - \sqrt{\frac{Pr}{Ra}} AB\left(\nabla \times \left(\nabla \times \mathbf{V}\right)\right)^{n,n-1} \right]$$

where $\mathbf{W}^{n+1}$ represents the velocity boundary condition at time step $n+1$. At the channel outlet, the discretization of Eq. (11) leads to:

$$\mathbf{W}^{n+1} = \frac{2\delta t}{3}\left[ \frac{4\mathbf{V}^n - \mathbf{V}^{n-1}}{2\delta t} - Re\sqrt{\frac{Pr}{Ra}}\frac{\partial \mathbf{V}^n}{\partial x} \right]$$

- *Computation of a predicted velocity* $\mathbf{V}^*$

The predicted velocity field $\mathbf{V}^*$ is computed implicitly from the momentum equation with the gradient of the preliminary pressure instead of that of the actual pressure $P_{dyn}^{n+1}$. The predicted velocity therefore satisfies the following problem:

$$\begin{cases} \rho^{n+1}\dfrac{3\mathbf{V}^* - 4\mathbf{V}^n + \mathbf{V}^{n-1}}{2\delta t} + AB\left(\rho \mathbf{V}.\nabla \mathbf{V}\right)^{n,n-1} = -\nabla \overline{P}_{dyn}^{n+1} + \sqrt{\dfrac{Pr}{Ra}}\Delta \mathbf{V}^* + \dfrac{1}{3}\sqrt{\dfrac{Pr}{Ra}}\nabla\left(\nabla.\mathbf{V}\right)^{n+1} \\ \qquad\qquad\qquad\qquad\qquad -\dfrac{1}{Fr}\left(\rho^{n+1} - \rho_i\right)\mathbf{e}_y \\ \mathbf{V}^* = \mathbf{W}^{n+1} \qquad \text{on } \partial\Omega \end{cases} \quad \text{in } \Omega$$

Here again, we have to solve Helmholtz equations with coefficients involving $\rho^{n+1}$ for each velocity component. As for the energy equation, the density $\rho^{n+1}$ is split into a constant part and a time-dependent part and Helmholtz equations with constant coefficients are solved iteratively for velocity components. The convergence is achieved when Max*(Resu, Resv)* $<10^{-13}$. This criterion is fulfilled after 3 or 4 iterations.

- *Correction step*

The converged velocity field $\mathbf{V}^*$ is then corrected by taking into account the pressure gradient at the current time step *n+1* so that the final velocity field satisfies the continuity equation (1). This correction is performed through the solution of the following Poisson problem for the intermediate variable $\varphi = 2\delta t \left( P_{dyn}^{n+1} - \bar{P}_{dyn}^{n+1} \right) \Big/ 3$ :

$$\begin{cases} \Delta \varphi = \nabla.\left( \rho^{n+1} \mathbf{V}^* \right) + \dfrac{3\rho^{n+1} - 4\rho^n + \rho^{n-1}}{2\delta t} & \text{in } \Omega \\ \dfrac{\partial \varphi}{\partial n} = 0 & \text{on } \partial\Omega \end{cases}$$

It must be noted that the above Poisson-Neumann problem must fulfill a compatibility condition to be solvable. Because of the inhomogeneous Dirichlet condition for the predicted velocity $\mathbf{V}^*$ at the channel outlet, this compatibility condition is not fulfilled. A renormalization of $\mathbf{V}^*$ at the outlet boundary was therefore performed before the solution of the Poisson-Neumann problem as proposed in Le and Moin (1994).

The actual velocity field and pressure at the current time step *n+1* are finally calculated in $\Omega \cup \partial\Omega$ by the formulae:

$$\mathbf{V}^{n+1} = \mathbf{V}^* - \frac{1}{\rho^{n+1}} \nabla \varphi \; , \; P_{dyn}^{n+1} = \bar{P}_{dyn}^{n+1} + \frac{3}{2\delta t} \varphi \, .$$

## 4. RESULTS AND DISCUSSION

Simulations were performed for a Reynolds number *Re=50.57*. The passage from the cold entry zone to the heated zone of the channel induces a perturbation of the flow. If the flow is stable, this perturbation decreases as it moves downstream and it leaves the system. On the other hand, when the flow is unstable, this perturbation grows and it gives rise to

16

thermoconvective patterns. Instantaneous temperature fields at several times are presented in order to show the spatio-temporal evolution of these structures.

First, the fluid was set at 1K above its critical temperature, which corresponds to a dimensionless distance to the critical point $\varepsilon=3.288\times10^{-3}$, and several values of the bottom wall heating were considered. These results were obtained in a channel with an aspect ratio $L'/H'=10$. Then, the influence of the proximity to the critical point was investigated in order to study the effect of the Prandtl number variations on the thermoconvective instability. In this case, in order to track further the different structures in the channel, we increased the aspect ratio to $L'/H'=15$.

### 4.1. Thermoconvective instabilities at 1K from the critical point

Computations were carried out for $\delta T'$ ranging from 0.02K up to 0.1K. Because of the divergence of the thermal expansion coefficient $\beta'$ and of the isobaric specific heat $C_p'$ near the critical point, these small temperature increases induce large Rayleigh numbers ranging from $1.05\times10^6$ to $5.23\times10^6$. Figure 3 shows the temperature fields at different calculation times for several values of $\delta T'$. In all the cases, instability appears in the form of thermal plumes which develop on the hot boundary layer. These structures are similar to those previously obtained for a supercritical fluid in the Rayleigh-Bénard configuration (Amiroudine et al., 2001; Chiwata and Onuki, 2001; Furukawa and Onuki, 2002; Furukawa et al., 2003; Amiroudine and Zappoli, 2003; Raspo et al., 2004; Accary et al., 2004; Accary et al., 2005a; Accary et al., 2005b). However, in a closed cavity, the bottom wall heating induces a piston effect that homogeneously increases the bulk temperature and that gives rise to a second unstable thermal boundary layer on the top cold wall. This is not the case in an open channel as it can be seen in Fig. 3. The couple $(t'_{ins}, x'_{ins})$ (where $t'_{ins}$ is the time corresponding to the beginning of the isotherms deformation and $x'_{ins}$ the axial position of the

first plume) which characterizes the instability onset is respectively (4*H'*, 1.22s), (3*H'*, 0.71s), (1*H'*, 0.33s) for *δT'*=0.02K, 0.04K and 0.1K. So the thermoconvective instability appears earlier and closer to the beginning of the heated zone when the Rayleigh number is increased. Furthermore, as the heating increases, the disturbances grow faster and the thermal plumes are larger.

Figure 3 also shows that the number and the development of the thermoconvective structures are different according to the value of *δT'*. While instability appears in the form of one or some plumes which move downstream during time for *δT'* about $10^{-2}$K (cases A and B), many structures develop in the whole channel for the largest heating (case C). In addition, in this last case, as the structures move downstream, new thermal plumes continuously appear near the beginning of the heated zone. This time evolution of the patterns may indicate that the structures are due to a convective instability in cases A and B and to an absolute instability in case C. Indeed, according to the previous studies for incompressible fluids, when the flow is convectively unstable, the initial perturbation locally grows, it moves downstream and it finally leaves the system. Hence, the thermoconvective structures cross the channel during time and the flow becomes stable again once they moved away. On the other hand, in the case of absolute instability, the initial perturbation locally grows but it also expands in the whole system so that the thermoconvective structures appear throughout the channel all the time although they move downstream: when a structure moves away, another one is locally generated in its place by the perturbation. However, results reported in literature for incompressible fluids showed that longitudinal rolls can never be absolutely unstable (Carrière and Monkewitz, 1999). Therefore, if the patterns in Fig. 3C are due to an absolute instability, they are likely transversal rolls. Further simulations are necessary to confirm this assumption. Several tests are possible in order to identify the type of the patterns that we obtain. First of all, transversal rolls are quasi two-dimensional structures whereas

longitudinal rolls are three-dimensional ones. Three-dimensional numerical simulations would therefore allow the precise identification of the structures. Another difference between transversal and longitudinal rolls concerns the instability thresholds: the critical Rayleigh number depends on the Reynolds and Prandtl numbers for the former whereas it doesn't for the latter. Therefore, the study of the influence of the Reynolds and Prandtl numbers on the critical value of *Ra* for the convective instability onset should allow to check our assumption.

### 4.2. Influence of the distance to the critical point on the thermoconvective instability

To determine the type of the structures obtained, we studied the influence of the Prandtl number on the instability threshold by varying the distance to the critical point. Indeed, the divergence of the thermal expansion coefficient and of the isobaric specific heat near this point leads to strong variations of the Prandtl number as is shown in table 1. The fluid is initially set at 5K above the critical temperature (the dimensionless distance to the critical point is then $\varepsilon=1.644\times10^{-2}$) instead of 1K. As a consequence, the Prandtl number becomes 5 times smaller. If the thermoconvective patterns observed are transversal rolls, this decrease must modify the threshold for convective instability. Indeed, linear stability analysis for incompressible fluids showed that the critical Rayleigh number for the onset of convectively unstable transversal rolls strongly depends on the value of the Prandtl number as is shown in Fig. 4. In this figure, the critical Rayleigh number $Ra_{c1}$ for convective instability onset was computed from the formula of Müller et al. (1992) for the two values of the Prandtl number $Pr=31.72$ and $Pr=6.28$. It can be seen that, for a same value of the Reynolds number, convective instability appears for smaller values of *Ra* as the Prandtl number decreases. We restricted the stability diagram to the range of small Reynolds numbers since the formula of Müller et al. was established using this assumption and experiments showed that transversal

rolls are only obtained for small values of *Re* for incompressible fluids and perfect gas. Nevertheless, the above results of linear stability analysis cannot be directly applied to our case since they were obtained with the assumption of incompressibility and constant physical properties, which is totally false for supercritical fluids.

Simulations were performed for a temperature increase $\delta T''$=0.27K, corresponding to a Rayleigh number $Ra$=5.23×10$^5$. Because of the strong decrease of the thermal expansion coefficient and of the isobaric specific heat as the distance to the critical point increases (see table 1), the Rayleigh number is much smaller than the smallest value that we considered at 1K from $T_c'$ (case A). Figure 5 shows the temperature fields obtained at two calculation times. It reveals that the thermoconvective structures develop much faster compared to case A of Fig. 3 and that they are also much larger. Results obtained in section 4.1 for $T_i'=T_c'+1K$ showed that, when the flow is unstable, the disturbances grow faster and the thermal plumes are larger as *Ra* increases. Therefore, the fast and strong growth of the perturbations in Fig.5 means that the value $Ra$=5.23×10$^5$ is much larger than the critical value $Ra_{c1}$ of the instability threshold for $Pr$=6.28. Two conclusions can be drawn from these results:

- first, contrary to what can be expected, the flow is convectively unstable for smaller values of *Ra* when moving away from the critical point. This is due to the decrease of the Prandtl number;

- secondly, the threshold of convective instability depends on the Prandtl number, since it depends on the distance to the critical point. Therefore, according to the previous studies (Müller et al., 1992; Carrière and Monkewitz, 1999), this result confirms that the thermoconvective structures observed are likely transversal rolls, since the critical Rayleigh number for longitudinal rolls is independent of *Pr*. However, experiments on incompressible fluids and perfect gas showed that transversal rolls only exist for small values of *Re* (*Re*<10). Therefore, the present results would indicate that, in a supercritical fluid, the transition

between transversal rolls and longitudinal rolls occurs for larger Reynolds numbers than for perfect gas or incompressible fluids.


## 5.  CONCLUSION

In this paper, the Poiseuille-Rayleigh-Bénard problem for a supercritical fluid, modeled by the Peng-Robinson equation of state, was studied for a Reynolds number $Re$=50.57. The temperature fields obtained in a channel of height $H'$=1mm revealed the existence of thermoconvective instabilities appearing in the form of thermal plumes, similar to those previously observed in supercritical fluids in the Rayleigh-Bénard configuration (Chiwata and Onuki, 2001; Amiroudine et al., 2001; Furukawa and Onuki, 2002; Furukawa et al., 2003; Amiroudine and Zappoli, 2003; Raspo et al., 2004; Accary et al., 2004; Accary et al., 2005a; Accary et al., 2005b). These thermal plumes develop on the hot boundary layer and then move downstream during time. Thus, contrary to the perfect gas case, for which the convective structures occupy the whole height of the channel, instability develops here on the fine thermal boundary layer along the heated zone. The temporal evolution of the patterns indicates that the instability is convective or absolute depending on the value of the Rayleigh number. As a consequence, since longitudinal rolls can never be absolutely unstable (Carrière and Monkewitz, 1999), the thermoconvective structures obtained are likely transversal rolls.

Moreover, the results obtained at different distances from the critical point showed that the critical Rayleigh number for the convective instability threshold depends on the Prandtl number. This variation of the critical Rayleigh number with the Prandtl number is also characteristic of transversal rolls according to previous studies (Müller et al., 1992; Carrière and Monkewitz, 1999).

Obviously, the results presented here are preliminary results and further simulations are necessary to confirm the type of structures that we obtained. In particular, simulations will be

performed to determine the convective instability threshold for various values of the Reynolds number as well as the Reynolds number for the transition between transversal rolls and longitudinal rolls. Three-dimensional computations will also be carried out.

**REFERENCES**

Accary, G., Raspo, I., Bontoux, P. and Zappoli, B., (2004) Three-dimensional Rayleigh-Bénard instability in a supercritical fluid, *C R Mécanique*, 332, pp. 209-216.

Accary, G., Raspo, I., Bontoux, P. and Zappoli, B., (2005a) Reverse transition to hydrodynamic stability through the Schwarzschild line in a supercritical fluid layer, *Phys. Rev. E*, 72, pp. 035301.

Accary, G., Raspo, I., Bontoux, P. and Zappoli, B., (2005b) Stability of a supercritical fluid diffusing layer with mixed boundary conditions', *Phys. Fluids*, 17, p. 104105.

Accary, G., Raspo, I. Bontoux P., and Zappoli, B., (2005c) An adaptation of the low Mach number approximation for supercritical fluid buoyant flows, *C R Mécanique*, 333, pp. 397-404.

Amiroudine, S., Bontoux, P., Larroudé, P., Gilly, B. and Zappoli, B., (2001) Direct numerical simulation of instabilities in a two-dimensional near-critical fluid layer heated from below, *J. Fluid Mech.*, 442, pp. 119-140.

Amiroudine, S. and Zappoli, B., (2003) Piston-effect-induced thermal oscillations at the Rayleigh-Bénard threshold in supercritical He, *Phys. Rev. Lett.*, 90, pp. 105301−105303.

Boukari, H., Shaumeyer, J. N., Briggs, M. E. and Gammon, R. W., (1990) Critical speeding up in pure fluids, *Phys. Rev. A*, 41, pp. 2260-2263.

Carrière, P. and Monkewitz, P. A., (1999) Convective versus absolute instability in mixed Rayleigh-Bénard-Poiseuille convection, *J. Fluid Mech.*, 384, pp. 243-262.

Chiwata, Y. and Onuki, A., (2001) Thermal plumes and convection in highly compressible fluids, *Phys. Rev. Lett.*, 87, pp. 144301.

Cocero, M. J., Martin, A., Mattea, F. and Varona, S., (2009) Encapsulation and co-precipitation processes with supercritical fluids: fundamentals and applications, *J. Supercrit. Fluid*, 47, pp. 546-555.

Erkey, C., (2009) Preparation of metallic supported nanoparticles and films using supercritical fluid deposition, *J. Supercrit. Fluid*, 47, pp. 517-522.

Evans, G. and Greif, R., (1989) A study of traveling wave instabilities in a horizontal channel flow with applications to chemical vapor deposition, *Int. J. Heat Mass Trans.*, 32, pp. 895-911.

Evans, G. and Greif, R., (1991) Unsteady three-dimensional mixed convection in a heated horizontal channel with applications to chemical vapor deposition, *Int. J. Heat Mass Trans.*, 34, pp. 2039-2051.

Evans, G. and Greif, R., (1993) Thermally unstable convection with applications to chemical vapor deposition channel reactors, *Int. J. Heat Mass Trans.*, 36, pp. 2769-2781.

Furukawa, A. and Onuki, A., (2002) Convective heat transport in compressible fluids, *Phys. Rev. E,* 66, pp. 016302.

Furukawa, A., Meyer, H., Onuki, A. and Kogan, A. B., (2003) Convection in a very compressible fluid: comparison of simulations with experiments, *Phys. Rev. E*, 68, pp. 56301–56309.

Gorbunov, A. A., Nikitin, S. A. and Polezhaev, V., (2007) Conditions of Rayleigh-Bénard convection onset and heat transfer in a near-critical medium, *Fluid Dyn.*, 42, pp. 704-718.

Haldenwang, P., Labrosse, G., Abboudi, S. and Deville, M., (1984) Chebyshev 3D spectral and 2D pseudospectral solvers for the Helmholtz equation, *J. Comput. Phys.*, 55, pp. 115-128.

Hugues, S. and Randriamampianina, A., (1998) An improved projection scheme applied to pseudospectral methods for the incompressible Navier-Stokes equations, *Int. J. Numer. Meth. Fluids*, 28, pp. 501-521.

Incropera, F. P., (1988) Convective heat transfer in electronic equipment cooling, *J. Heat Trans.*, 110, pp.1097-1111.

Le, H. and Moin, P., (1994) Direct numerical simulation of turbulent flow over a backward-facing step, *Report TF-58, Thermosciences Division, Dept. of Mech. Eng. Stanford University*.

Müller, H. W., Lücke, M. and Kamps, M., (1992) Transversal convection patterns in horizontal shear flow, *Phys. Rev. A*, 45, pp. 3714-3726.

Nicolas, X., (2002) Bibliographical review on the Poiseuille–Rayleigh–Bénard flows: the mixed convection flows in horizontal rectangular ducts heated from below, *Int. J. Therm. Sci.*, 41, pp. 961-1016.

Onuki, A., Hao, H. and Ferrell, R. A., (1990) Fast adiabatic equilibration in a single-component fluid near the liquid-vapor critical point, *Phys. Rev. A*, 41, pp. 2256-2259.

Ouazzani, J. and Garrabos, Y., (2007) A new numerical algorithm for low Mach number supercritical fluids, Retrieved october 2007 from http://hal.archives-ouvertes.fr/index.php?halsid=dberarqjkcq1uhun20aqd960s7&view_this_doc=hal-00142988&version=1.

Paolucci, S., (1982) On the filtering of sound from the Navier-Stokes equations, *Technical report, Sandia National Laboratories USA, SAND82-8257.*

Raspo, I., Hugues, S., Serre, E., Randriamampianina, A. and Bontoux, P., (2002) A spectral projection method for the simulation of complex three - dimensional rotating flows, *Comput. Fluids,* 31, pp. 745-767.

Raspo, I., Zappoli, B. and Bontoux, P., (2004) Unsteady two-dimensional convection in a bottom heated supercritical fluid, *Comptes Rendus de Mécanique*, vol. 332, pp. 353-360.

Raspo, I. and Ouazzani, J., (2009) Un algorithme faible nombre de Mach pour la simulation des écoulements de fluides supercritiques par des méthodes spectrales, *Proc. of the 19th Congrès Français de Mécanique*, C Rey, P. Bontoux, A. Chrysochoos Eds., ISSN 2103_6225, paper 337-S05.

Reverchon, E. and De Marco, I., (2006) Supercritical fluid extraction and fractionation of natural matter, *J. Supercrit. Fluid*, 38, pp. 146-166.

Spall, R. E., (1996) Unsteady mixed convection in horizontal ducts with applications to chemical vapor deposition processes, *Int. Commun. Heat Mass*, 23, pp. 115-122.

Zappoli, B., Bailly, D., Garrabos, Y., Le Neindre, B., Guenoun, P., and Beysens, D., (1990) Anomalous heat transport by the piston effect in supercritical fluids under zero gravity, *Phys. Rev. A*, 41, pp. 2264-2267.

Zappoli, B., Amiroudine, S., Carlès, P. and Ouazzani, J., (1996) Thermoacoustic and buoyancy-driven transport in a square side-heated cavity filled with a near-critical fluid, *J. Fluid Mech.*, 316, pp. 53-72.

**Figure captions**

**Figure 1:**    Linear stability diagram of the PRB flow for incompressible fluids showing the two instability thresholds for transversal rolls (established from formulae given by Müller et al. (1992) for *Pr*=0.6567). The basic flow is stable below the threshold of linear stability (*Ra*<*Ra$_{c1}$*), transversal rolls are convectively unstable for *Ra$_{c1}$*<*Ra*<*Ra$_{c2}$* and absolutely unstable for *Ra*>*Ra$_{c2}$*.

**Figure 2:**    Channel geometry with top and bottom thermal boundary conditions.

**Figure 3:**    Temperature fields for *T$_i$'*=*T$_c$'*+1K (*Pr*=31.72) and several values of *Ra*.

**Figure 4:**    Linear stability diagram of the PRB flow for incompressible fluids showing the instability threshold for convectively unstable transversal rolls (established from the formula given by Müller et al. (1992)) for two values of the Prandtl number *Pr*. The critical Rayleigh number *Ra$_{c1}$* for the onset of convective instability increases with *Pr*.

**Figure 5:**    Temperature field for *T$_i$'*=*T$_c$'*+5K (*Pr*=6.28) and *Ra*=5.23×10$^5$.

**Table titles**

**Table 1:** Thermodynamic properties and Prandtl number at 1K and 5K above the critical point.

Table 1

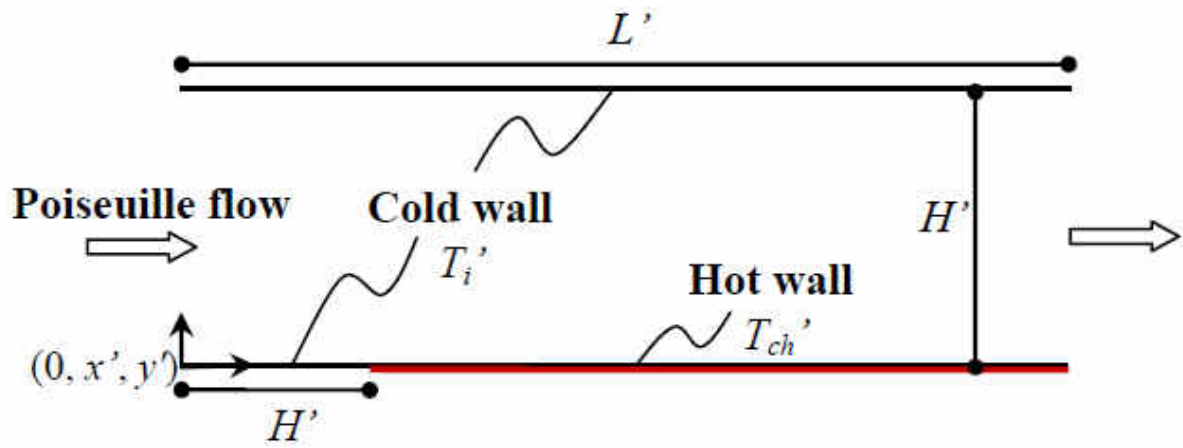| $T_i' - T_c'$ (K) | $\beta'$ (K$^{-1}$) | $C_p'$ (J/kg/K) | $Pr$ |
|---|---|---|---|
| 1 | 0.82199 | 42803.48 | 31.72 |
| 5 | 0.15334 | 8478.77 | 6.28 |

Figure 1

Figure 2

Figure 3
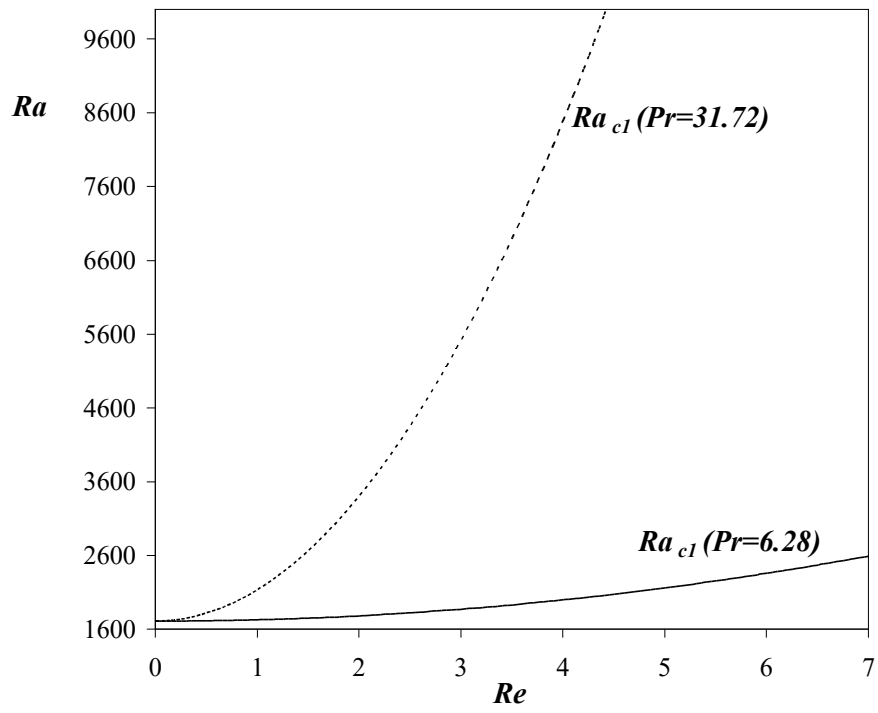


*A*      $\delta T'=2\times10^{-2}$K *(Ra=1.05×10^6)*

$t'=0.83$s

$t'=1.22$s

$t'=1.26$s

$t'=1.61$s

*B*      $\delta T'=4\times10^{-2}$K *(Ra=2.09×10^6)*

$t'=0.45$s

$t'=0.72$s

$t'=1.00$s

$t'=1.28$s

*C*      $\delta T'=10^{-1}$K *(Ra=5.23×10^6)*

$t'=0.33$s

$t'=0.47$s

$t'=0.61$s

$t'=0.89$s

Figure 4

Figure 5



$t'$=1.14s

$t'$=1.26s

Figure 5